

## Nitrogen-rich carbon nitride inducing electron delocalization of Co-N<sub>4</sub> site to enhance electrocatalytic carbon dioxide reduction

Jofrey Jackson Masana <sup>a,b,1</sup>, Jiayong Xiao <sup>a,1</sup>, Hui Zhang <sup>a</sup>, Xiaoying Lu <sup>c</sup>, Ming Qiu <sup>a,\*</sup>, Ying Yu <sup>a,\*</sup>

<sup>a</sup> Institute of Nanoscience and Nanotechnology, College of Physical Science and Technology, Central China Normal University, Wuhan 430079, China

<sup>b</sup> Mwalimu Julius K. Nyerere University of Agriculture and Technology, P.O Box 976, Musoma, Tanzania

<sup>c</sup> Faculty of Science and Technology, Technological and Higher Education Institute of Hong Kong, Hong Kong, China

### ARTICLE INFO

#### Keywords:

Electrochemical reduction of CO<sub>2</sub>  
Nitrogen-rich carbon nitride  
Cobalt phthalocyanine  
Electron delocalization  
Co-N<sub>5</sub> catalytic site

### ABSTRACT

Cobalt phthalocyanine (CoPc) is an appealing electrocatalyst for CO<sub>2</sub> reduction. However, its catalytic performance is limited by instability and low conductivity. Herein, theoretical calculations reveal that nitrogen-rich carbon nitride, as a promising Supporting material, can help to tune the electronic structure of CoPc and then enhance its stability and conductivity by inducing electron delocalization of Co-N<sub>4</sub> sites for the formation of Co-N<sub>5</sub>, achieving a superior electrochemical reduction of CO<sub>2</sub>. Inspired by this prediction, we prepared nitrogen-rich carbon nitride that coordinated with Co-N<sub>4</sub> through axial N coordination under 400 °C, forming an atomically dispersed Co-N<sub>5</sub> catalytic site. The synthesized catalyst demonstrates excellent performance in CO<sub>2</sub> conversion to CO with >99 % selectivity at a current density of ~ 5.3 mA cm<sup>-2</sup>, which can remain for 40 h. These findings provide a strategy for regulating catalytic sites and shed light on expanding the applications of low-cost carbon nitride materials at mild heat-treatment temperatures.

### 1. Introduction

CO<sub>2</sub> can be utilized as a renewable feedstock in electrochemical devices for long-term energy storage, either as synthetic fuels or fuel precursors (such as CO, CH<sub>3</sub>OH, and CH<sub>4</sub>) [1–3]. A cost-efficient route to transform CO<sub>2</sub> into desired products in industrial-scale may help to mitigate the environmental impact of huge CO<sub>2</sub> emissions. Electrochemical reduction of CO<sub>2</sub> (CO<sub>2</sub>RR) is one of an alluring approaches that can perform this functionality under mild conditions [4–6]. However, the practical application of this process remains a challenge due to lack of efficient electrocatalysts with good stability and high product selectivity [7,8], which is preferred to simplify product purification and enhance energy conversion efficiency [9].

Molecular complexes with nitrogen-coordinated centers (M-N<sub>4</sub>) are considered potential catalysts for CO<sub>2</sub>RR due to their ability to allow fine-tuning of the primary and secondary coordination spheres by manipulating chelating environment and ligands' steric and electronic effects [9–14]. Several studies have reported altering their reaction mechanisms for catalytic performance improvement by integrating the

nitrogen-coordinated centers into organic media such as covalent organic framework (COF), poly(4-vinylpyridine) (P4VP), or metal-organic framework (MOF) [15–18]. In these organic media, cobalt phthalocyanine (CoPc) has been widely investigated due to its high activity and selectivity toward CO [1,19]. However, the catalytic performance of CoPc is often limited by its aggregation and low conducting nature, which leads to instability, low current density and significant co-generation of H<sub>2</sub> [17,18]. Incorporating CoPc into high conductive supports such as carbon nanotubes [12,20–22] and nitrogen-doped carbon [23,24] for CO<sub>2</sub> to CO conversion has demonstrated impressive performance. The incorporation of CoPc is achieved through π-π interaction between the CoPc macrocyclic complexes and these supports, which is not a direct interaction between the catalytic sites and supports [12,17,25]. Recent research finds that direct interaction can significantly modify electronic configurations of catalytic sites and result in more favored CO<sub>2</sub> adsorption/desorption for improving CO<sub>2</sub> electro-reduction [25].

Due to their featured peculiar structure and electronic properties, nitrogen-rich carbon nitrides have emerged as promising Supporting

\* Corresponding authors.

E-mail addresses: [qium@mail.ccnu.edu.cn](mailto:qium@mail.ccnu.edu.cn) (M. Qiu), [yuying01@mail.ccnu.edu.cn](mailto:yuying01@mail.ccnu.edu.cn) (Y. Yu).

<sup>1</sup> These authors contributed equally to this work.



materials that can bring salient features when composited with metals [26–31]. Under mild heat-treatment temperature, nitrogen-rich carbon nitrides have s-triazine rings that consist  $6\pi$ -electron system, enabling them to possess a layered structure that stabilizes guest chemical species between layers [32]. Impressively, the stable  $6\pi$ -electron system of the s-triazine can be retained up to a temperature of 400 °C though it quickly decomposes over 500 °C [32], through which the surface composition and electronic structure of nitrogen-rich carbon nitrides can be controlled [33,34]. Congruently, the catalytic activity of CoPc is also related to heat-treatment temperature. According to literature, CoPc remains intact for heat treatment up to 400 °C [35–38]. During this process, it undergoes a polymerization reaction, which associates with the initial release of axially coordinated molecules with the  $\text{Co}^{2+}$  center, such as water,  $\text{CO}_2$  and/or CO accompanied by a reaction of remaining macrocycle with the respective substrate. Between 430 °C and 630 °C, the polymerization of the phthalocyanine unit is completed, and the decomposition of the CoPc-like polymer, including Co-N<sub>4</sub>, is responsible for the weight loss [38–40]. Thus, it is possible to modulate the Co-N<sub>4</sub> sites and, consequently, electronic structure with suitable Supporting materials such as nitrogen-rich carbon nitrides under this mild heat-treatment temperature of ~ 400 °C. However, the study on electrocatalysis by metal phthalocyanines anchored onto nitrogen-rich carbon nitrides for  $\text{CO}_2\text{RR}$  is rarely elaborated.

Herein, our theoretical calculations revealed that CoPc connected with nitrogen-rich carbon nitride support through axial nitrogen coordination could induce electron delocalization to boost the rapid formation of \*COOH intermediate for remarkable  $\text{CO}_2\text{RR}$  performance. Experimentally, we investigated CoPc and nitrogen-rich carbon nitrides interaction under mild heat-treatment temperature and explored their electrocatalysis performance in close neutral electrolytes for  $\text{CO}_2\text{RR}$ . That is, nitrogen-rich carbon nitride support (melamine, polyethylene glycol, and triblock copolymer pluronic, simplified as MPF) was synthesized in a facile way under a mild temperature of 400 °C. A Co-N<sub>5</sub> catalytic site was confirmed by X-ray absorption spectroscopy. The Co-N<sub>5</sub>/MPF affords  $\text{CO}_2\text{RR}$  to CO with >99 % selectivity at  $-5.3 \text{ mA cm}^{-2}$  and  $-0.84 \text{ V}$  vs. reversible hydrogen evolution (RHE), which also has long-term stability and exhibits >95 % selectivity for 40 h in a customized gastight H-type glass cell device.

## 2. Experimental section

### 2.1. Chemicals and materials

Ammonia aqueous solution ( $\text{NH}_3\text{-H}_2\text{O}$ , 25–28 wt. %), ethanol ( $\text{CH}_3\text{CH}_2\text{OH}$ , AR), *N,N*-Dimethylformamide (DMF, AR), polyethylene glycol, PEG-20000 (99 %) and melamine (99 %), potassium bicarbonate (99.999 %) were all purchased from Sinopharm Chemical Reagent Co., Ltd. Triblock copolymer pluronic F127 (PEO<sub>106</sub>PPO<sub>70</sub>PEO<sub>106</sub>) ( $M_w = 13,000$ ) and cobalt phthalocyanine (CoPc, 90 %) were purchased from Shanghai Macklin Biochemical Co., Ltd. The carbon cloth WOS1011 (thickness of 0.33 mm) was purchased from CeTech Co., Ltd. Nafion 117 membrane was purchased from Gaossunion. 18.2  $\text{M}\Omega$  ultrapure water was obtained from milli-Q system. High purity Argon gas (Ar, 99.9999 %) and carbon dioxide ( $\text{CO}_2$ , 99.995 %) were from XiangYu company (China). All chemicals and solvents were used as received.

### 2.2. Synthesis of MPF

Synthesis of MPF was done via reaction conditions previously reported [32,33,41,42] with some modification. In a typical synthesis of MPF, 2.5 ml aqueous ammonia solution (25 ~ 28 wt. %) was diluted with 5 ml deionized water to control the morphology of the MPF. Then, 2.5 ml of the above diluted solution, 50 ml of ethanol, and 20 ml of deionized water were mixed and stirred for 30 min at 30 °C. Subsequently, 1.95 g of F127 and 1.95 g of PEG-20000 were added to the above mixture and stirred for another 30 min. After that, 1.95 g of

melamine was added. The mixture was stirred for 24 h at 30 °C continually. Then, the above mixture solution was transferred into 100 ml Teflon-lined stainless autoclaves and heated at 120 °C for 12 h. The as-obtained white precipitate was centrifuged and washed with ethanol and deionized water for three times, respectively. Subsequently, as-obtained white precipitate was dried in an oven at 60 °C for 12 h. Finally, the MPF was prepared by heating the dried powder at 400 °C for 2 h at 2 °C/min to form nitrogen-rich carbon nitride for supporting CoPc.

### 2.3. Synthesis of Co-N<sub>5</sub>/MPF

In a typical synthesis of CoPc/MPF, 20 mg of CoPc and 50 mg of MPF were mixed in 30 ml DMF separately by sonication for at least 1 h. Further, CoPc-DMF suspension was added to the MPF-DMF. The mixed suspension was further stirred for 24 h at 30 °C. The obtained CoPc/MPF by centrifugation (9000 rpm for 5 min) was washed with DMF for many times until the solution became colourless, followed by a drying process in a vacuum oven at 60 °C for 12 h. The sample CoPc/MPF and melamine were mixed by grinding with the mass ratio of 1:5, and then the ground mixture was annealed in a tube furnace at 400 °C temperature for 2 h with a heating rate of 2 °C/min under flowing Ar gas to form CoPc/MPF-400 °C (Co-N<sub>5</sub>/MPF). The as-obtained samples were directly used without any post-treatment. For comparison, standard CoPc was annealed at 400 °C to form CoPc-400 °C and CoPc/MPF at 500 °C and 600 °C to form CoPc/MPF-500 °C and CoPc/MPF-500 °C, respectively, under similar conditions. To optimize hybrid catalyst, melamine was added during the pyrolysis process. The reason is that at this temperature, melamine crystalline changes to amorphous graphite-like carbon nitride compound [33], which probably will not affect the MPF structure. More significantly, melamine could modify the unstable carbon species for the formation of carbon nitride bonding by triazine, which is crucial for N doping source and is produced from melamine decomposition during annealing [43].

### 2.4. Characterization

XRD data were collected using a PANalytical B.V. X'Pert PRO X-ray diffractometer with a Cu-K $\alpha$  irradiation source. Raman scattering data were recorded on LabRAM HR JY-Evolution microscope using a 532 nm argon-ion laser. X-ray photoelectron spectroscopy (XPS) was measured by Thermo ESCALAB250Xi. FTIR measurements were performed by the Thermal iS50. UV-vis measurements were performed by PerkinElmer Lambda 750S. SEM images were obtained on a JEOL JSM-6700F scanning electron microscope at 6 kV with the software package for automated electron tomography. TEM images were achieved on Tecnai G2 F30. XAS spectra at Co K-edge were measured in transmission mode at XAFCA beamline of Singapore Synchrotron Light Source (SSL) (The storage ring was working at the energy of 2.5 GeV with an average electron current of 150 mA). The cobalt XAFS raw data processing was carried out using ATHENA (Demeter 0.9.26, an interface to IFEFFIT) and ARTEMIS (Demeter 0.9.26) by the standard procedures [44]. The  $k^3$ -weighted  $\chi(k)$  data in the  $k$ -space ranging from 3.0 to 10.2  $\text{\AA}^{-1}$  were Fourier-transformed to real (R) space using a Hanning window ( $dk = 1.0 \text{ \AA}^{-1}$ ) to separate the EXAFS contributions from different coordination shells. To obtain the detailed structural parameters around the Co atom in as-prepared samples, quantitative curve fittings were carried out for the Fourier-transformed  $k^3\chi(k)$  in R-space using the ARTEMIS module of IFEFFIT. The Debye-Waller factor ( $\sigma^2$ ) and bond length (R) were treated as adjustable parameters during curve fittings. The Morlet wavelet was chosen as the mother wavelet for basic functions, and the parameters ( $\sigma = 1$ ,  $\eta = 5$ ) were used to achieve better resolution in the wave vector  $k$ .

## 2.5. $\text{CO}_2$ reduction evaluation

$\text{CO}_2\text{RR}$  was conducted at ambient temperature and pressure in a customized gastight H-type glass cell separated by a Nafion 117 membrane (Fuel Cell Store) with a three-electrode system. A piece of platinum foil ( $1 \text{ cm} \times 1 \text{ cm} \times 0.2 \text{ cm}$ ) and Ag/AgCl electrode (KCl sat.) served as counter and reference electrode, respectively. The working and reference electrodes were placed in the cathode chamber with a 0.5 M  $\text{KHCO}_3$  solution, while the counter electrode was placed in the anode chamber. A CHI 660e potentiostat was employed to record electrochemical responses. All potentials measured were calibrated to the RHE scale as follows:  $V_{\text{RHE}} = V_{\text{Ag/AgCl (KCl sat.)}} + 0.197 \text{ V} + 0.059 \text{ V} \times \text{pH}$ . Ultrahigh purity  $\text{CO}_2$  (99.99 %) was purged into the 0.5 M  $\text{KHCO}_3$  solution for at least 30 min to achieve a  $\text{CO}_2$ -saturated 0.5 M  $\text{KHCO}_3$  aqueous solution ( $\text{pH} = 7.4$ ). The electrode was held at a constant bias using chronoamperometry for 5 C charge, after which a 500  $\mu\text{L}$  gas sample was taken by a syringe (Hamilton) from the headspace. Then, the gas sample was injected into a gas chromatograph instrument (GC-2014, Serial No. C11484403556 SA, /Shimadzu, Japan) equipped with a flame ionization detector (FID) for detection of organic compounds and a gas chromatograph instrument (Serial No C11485013433 SA, Shimadzu, Japan) equipped with a thermal conductivity detector (TCD) for detection of inorganic gases (for more details, see [Supporting information](#)).

## 2.6. Computation methods

By using Vienna *ab initio* simulation package (VASP) [45], all density functional theory (DFT) calculations were performed with projector augmented wave (PAW) potential method to apply first-principles-based quantum mechanics simulations [46]. The generalized gradient approximation (GGA) of Perdew–Burke–Ernzerhof (PBE) was employed to describe the exchange-correlation energy between electron–ions [47]. In this work, the cut-off energy of the plane wave was set as 500 eV, and the k-point grid was set as  $3 \times 3 \times 1$  to optimize the geometric structure. The convergence criterion was set to be  $0.02 \text{ eV } \text{\AA}^{-1}$  for the force and  $10^{-5} \text{ eV}$  per atom for energy. Smearing method was set to ISMEAR = 0 with a Sigma value of 0.05 eV, which determined the electron distribution near the Fermi level (for more details, see [supporting information](#)).

## 3. Results and discussion

### 3.1. Simulations, material synthesis, and morphology characterization

To explore the effectiveness of CoPc and MPF composite, we firstly performed DFT calculations by connecting CoPc with MPF support through axial N coordination, as illustrated in Fig. 1a, b, and S1. It should be stressed that CoPc at  $400 \text{ }^\circ\text{C}$  remains intact, as detailed discussed in the introduction section. For the purpose of illuminating the structural stability of CoPc at  $400 \text{ }^\circ\text{C}$ , the influence of the temperature ( $400 \text{ }^\circ\text{C}$ ) to the Co-N<sub>4</sub> active site was further investigated theoretically (Fig. S2). Thus, it was considered that standard CoPc and CoPc-400 °C have similar structures. In principle, generation of \*COOH intermediate is a key factor for promoting  $\text{CO}_2\text{RR}$  [42,48]. Considering this, the charge difference was calculated to investigate the interaction between CoPc, and Co-N<sub>5</sub>/MPF in terms of adsorbed \*COOH intermediate. Fig. 1b demonstrates that the interaction between CoPc and MPF through axial N coordination leads to electron delocalization between Co-N<sub>5</sub> site and the support compared to that of CoPc sites without MPF substrate, which can be termed as electron-withdrawing effect [49]. To explore more about this effect, the Bader charge and planar-averaged charge density difference were calculated, as shown in Fig. S1. The Bader charge analysis disclosed that the electrons at Co site in Co-N<sub>5</sub>/MPF are partially depleted ( $-1.06|\text{e}|$ ) compared to that of CoPc ( $-1.00|\text{e}|$ ) due to electron transfer to MPF support ( $+0.19|\text{e}|$ ). It was found that Co-N<sub>5</sub>/MPF transfers more charge to the intermediate \*COOH ( $+0.20|\text{e}|$ ) than that transferred by CoPc ( $+0.14|\text{e}|$ ) without MPF, in accordance with the results of planar-averaged charge density difference (Fig. S1). Thus, this effect would influence the binding strength of the reaction intermediates to the active site [42]. Consequently, the lowered energy barrier of \*COOH intermediate formation over Co-N<sub>5</sub>/MPF promotes its fast reaction kinetics for the  $\text{CO}_2\text{RR}$  compared to that of CoPc.

The analysis of the projected density of states (PDOS) in Fig. 1b clarified that coordination interaction between CoPc and MPF makes the Fermi level of Co-N<sub>5</sub>/MPF shift farther than that of its counterpart owing to the robust coupling of the d states of Co with p states of N atoms, thereby increasing its states delocalization degree [49]. In addition, the total density of states (TDOS) shows considerable states density of Co-N<sub>5</sub>/MPF across the Fermi level, suggesting more electron occupancy states with high electronic conductivity and carrier density near the Fermi level than that of CoPc, which could result in the improvement of its charge transfer ability. For model Co-N<sub>5</sub>/MPF, the states

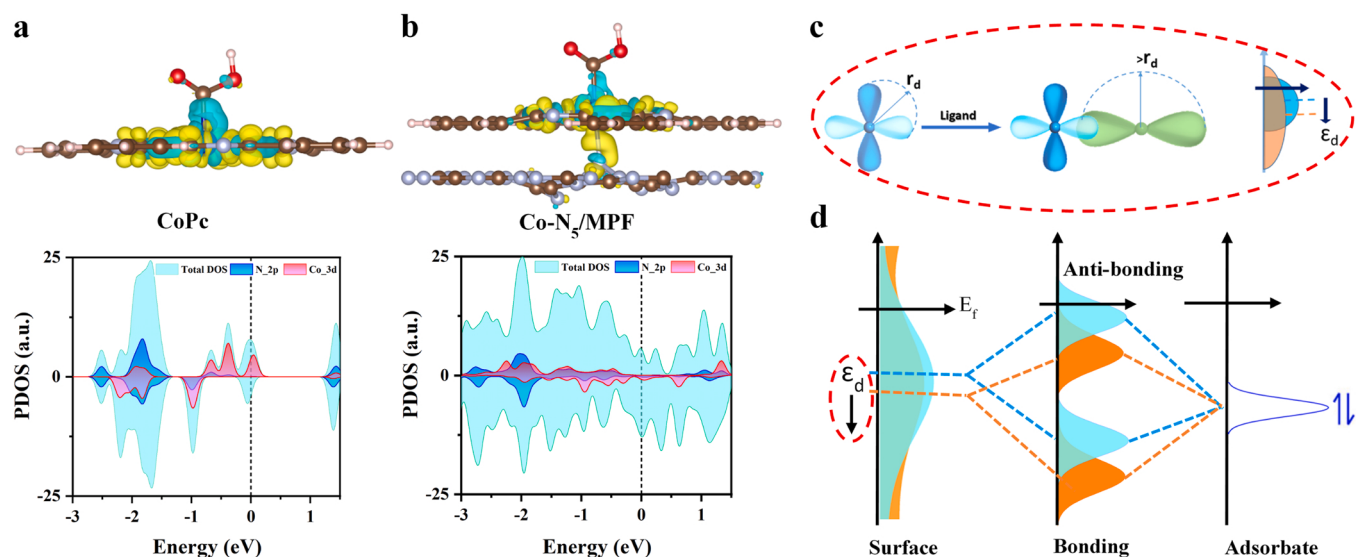


**Fig. 1.** (a, b) Charge density differences for \*COOH intermediate adsorbed on optimized structures of CoPc and Co-N<sub>5</sub>/MPF with corresponding PDOS. (c) Overlap between d-states and p-orbitals of adsorbate leading to a change in the d-bandwidth. (d) Illustration of the d-band model of chemisorption.

hybridization between *d*-orbitals of Co atom and *p*-orbitals of N atoms (Fig. 1c), which then splits into bonding and anti-bonding states (Fig. 1d), is anticipated to facilitate catalytic adsorption. Moreover, farther increased *d*-band center energy level with flatter bands in Co-N<sub>5</sub>/NHPCs indicates that anti-bonding states are filled with more states than that in CoPc, which would influence adsorption energy of CO<sub>2</sub> intermediate on the active site [50–52]. Therefore, the MPF can affect the local catalytic site of CoPc, which leads to optimizing its catalytic site and enhancing the electron delocalization, resulting in accelerated reaction kinetics and boosting the CO<sub>2</sub>RR performance significantly [53,54].

Inspired by DFT calculations, CoPc molecule was atomically dispersed on MPF support through a simple strategy, as shown in Fig. 2a. Firstly, MPF substrate was obtained through the cooperation of melamine, PEG-20000, and F127, which was then subjected to 400 °C temperature to form amorphous graphite-like organic polymer [33] (Fig. S3a~c). Subsequently, CoPc molecule was immobilized in MPF by a simple reaction of CoPc in MPF aqueous dispersed system followed by heat treatment (see experimental section), whereby the Co-N<sub>5</sub>/MPF catalyst was obtained. The scanning electron microscope (SEM), transmission electron microscope (TEM), X-ray powder diffraction (XRD), and elemental mapping of the Co-N<sub>5</sub>/MPF catalysts were characterized to ensure uniform dispersion of CoPc molecules in MPF, and rod-like shaped morphology was observed (Figs. 2b and S4). The TEM images and the energy-dispersive X-ray spectroscopy (EDX) maps in Fig. 2c showed the good distributions of C, N and Co elements and matched the rod-shaped morphology, confirming highly dispersed CoPc in forming Co-N<sub>5</sub>/MPF catalyst (Co, 1.35 at. %, Table S1). The High-resolution TEM (HRTEM) image revealed no nanoparticles formed in the hybrid catalyst (Fig. 2d, enlarged inset image shows bright spot corresponding to Co atom), and the prepared sample was not well crystallized. To further confirm the high disparity of CoPc in MPF, aberration-corrected high-angle annular dark field scanning transmission electron microscopy (HAADF-STEM) imaging was performed, overlapping EDX map (Fig. S4) of Co atom in Co-N<sub>5</sub>/MPF showed homogeneous distribution of Co atoms across the entire MPF support. To explore the coordination interaction features, analysis of Fourier transform infrared (FTIR) spectrum was conducted (Fig. 2e). The strong band at around 1250–1600 cm<sup>-1</sup> and 1630 cm<sup>-1</sup> over MPF corresponds to the stretching modes of the cyanogen ring (C<sub>3</sub>N<sub>3</sub>) and the aromatic C=N, respectively [55,56], suggesting that the material comprises sp<sup>2</sup> CN. A vibrational band in the range 3180–3500 cm<sup>-1</sup> is attributed to stretching of amino groups (N-H), indicating presence of intermolecular hydrogen bonding in the MPF [55]. After immobilization reaction, there was no obvious difference between the Co-N<sub>5</sub>/MPF and MPF structure, implying the original MPF structure was maintained. However, several new peaks appeared in the FTIR spectra of Co-N<sub>5</sub>/MPF (Fig. 2e). The characteristic peak at 1630 cm<sup>-1</sup> of MPF stretched to 1652.9 cm<sup>-1</sup> in Co-N<sub>5</sub>/MPF, revealing there might be bond coordination between CoPc and MPF [57]. In addition, absorption band peak related to NH stretching in Co-N<sub>5</sub>/MPF became weaker and broader relative to that of MPF due to the presence of hydrogen bonding, further suggesting the coordination between CoPc and MPF. Impressively, the characteristics peak centered at 804 cm<sup>-1</sup> in MPF, corresponding to 6π-electron system of the s-triazine, shifted to 811 cm<sup>-1</sup> in Co-N<sub>5</sub>/MPF, implying the strong interaction between CoPc and MPF. As previously pointed out, carbon nitride retains s-triazine ring at mild temperature. Thus, the existence of s-triazine ring, chemical species in the MPF, would stabilize Co atom and consequently enhance the stability of the Co-N<sub>5</sub>/MPF catalyst.

The corresponding XRD patterns of MPF and Co-N<sub>5</sub>/MPF are shown in Fig. 2f. For MPF, the diffraction peak at ~ 13° was attributed to the periodic s-triazine units, and ~ 27.5° belonged to the diffraction of the layered material {(C<sub>3</sub>N<sub>3</sub>)<sub>2</sub>(NH)<sub>3</sub>}<sub>n</sub> [32,58]. The diffraction peaks of Co-N<sub>5</sub>/MPF were quite different from those of MPF. The gradual decrease of the intensity for the 27.5° peak after immobilization reaction demonstrated the destruction of hydrogen bonds in the intralayer of

hydrogen bonds framework [59].

Also, the peak at 13° almost vanished, inferring the disordered intralayer s-triazine structures existed within the Co-N<sub>5</sub>/MPF structure. The peaks of CoPc were very hard to be observed in Co-N<sub>5</sub>/MPF, suggesting good interaction between CoPc and MPF, which might prevent CoPc molecules from agglomeration via π-π stacking to form crystal [24]. However, to demonstrate that CoPc was mobilized in MPF, we loaded MPF with 30 mg of CoPc and heated it at 400 °C. As expected, all diffraction peaks of CoPc were detected, suggesting that the structure of CoPc in Co-N<sub>5</sub>/MPF had not changed (Fig. S3d). Instead, it was highly dispersed due to a well-optimized amount of CoPc (20 mg), as confirmed by HRTEM and HAADF-STEM results (Figs. 2d and S4). To further elucidate the influence of temperature on standard CoPc, XRD patterns for standard CoPc and CoPc-400 °C were compared, and little difference was observed (Fig. S3e).

Solid UV-vis was performed to explore structural changes. UV-vis spectra of Co-N<sub>5</sub>/MPF and CoPc-400 °C displayed distinctive B-band and Q-band of phthalocyanines, as shown in Fig. 2g. Noticeably, Co-N<sub>5</sub>/MPF exhibited a red shift in Q-band absorption area (the insert in Fig. 2g) relative to CoPc-400 °C, suggesting that the environment coordination of CoPc in MPF probably might have changed. Besides, it can be observed that Co in CoPc-400 °C displays no absorption band beyond wavelength 700 nm suggesting no defects or impurities were generated during the preparation process. In contrast to the CoPc-400 °C, the Co in Co-N<sub>5</sub>/MPF exhibits noticeable enhancement in light absorption in the wavelength beyond 700 nm with an absorption peak centered at around 741 nm (Fig. 2g and S5), which is attributed to the surface plasmon resonance (SPR) of ligand-to-metal [60,72,73]. These results suggest an additional ligand bond to CoPc. To confirm that the emerging absorption peak comes from coordination interaction, UV-vis spectrum of standard CoPc was analysed and compared with that of CoPc-400 °C (Fig. S5). No significant differences were found. Notably, these results provide further solid evidence for the coordination interaction between CoPc and MPF, and emerging absorption peak of CoPc in Co-N<sub>5</sub>/MPF might be influenced by the additional fifth ligand.

To further characterize the Co-N<sub>5</sub>/MPF hybrid, Raman spectroscopy was used, as shown in Fig. 2h. It can be seen that vibrational peaks of MPF were discerned in the spectrum. It is noted that the CoPc vibrational features were not observed for the hybrid material, which might be due to the small amount of CoPc in the hybrid. The CoPc content in the hybrid was adjusted from 20 to 30 mg. The Raman spectroscopy results of the corresponding materials are shown in Fig. S6. With a CoPc content of 30 mg Raman spectrum shows most of the CoPc vibrational features, suggesting that CoPc aggregates have formed with such a high loading [12,24].

The surface catalytic environment of Co-N<sub>5</sub>/MPF was probed by XPS, as presented in Fig. 3 and S7. From Fig. 3a, the high-resolution XPS spectrum for Co 2p shows pair peaks of Co<sup>2+</sup> (780.9 and 796.1 eV) and Co<sup>3+</sup> (782.0 and 796.9 eV) for CoPc-400 °C, Co<sup>2+</sup> (780.5 and 795.9 eV) and Co<sup>3+</sup> (781.9 and 796.8 eV) for Co-N<sub>5</sub>/MPF [21,24,42]. The peak positions of Co 2p in Co-N<sub>5</sub>/MPF catalyst shifted to lower binding energy, suggesting electronic coordination between Co atoms and MPF. To further explore the negative shift of Co 2p, XPS spectra of the physical mixing of CoPc and MPF were carefully analysed (Fig. S7). It was found that the binding energy of the peak Co 2p is almost the same as that of CoPc-400 °C, suggesting that in physical mixing, the electronic interaction between the CoPc and MPF is too weak to change the binding energy of peak Co 2p. In addition, the full width at half maximum (FWHM) was analysed to investigate whether there is chemical bonding between the central metal Co atom and MPF substrate. It is expected that any chemical bonding with the central metal Co atom would be observed as an increase in the lattice disorder [74], which would be demonstrated as an increase of the FWHM of the Co peak. As expected, Co-N<sub>5</sub>/MPF showed broader FWHM (Table S2) than all its counterparts indicating additional chemical bonding presence. Thus, the lower binding energy shift of Co in Co-N<sub>5</sub>/MPF may be attributed to an extra

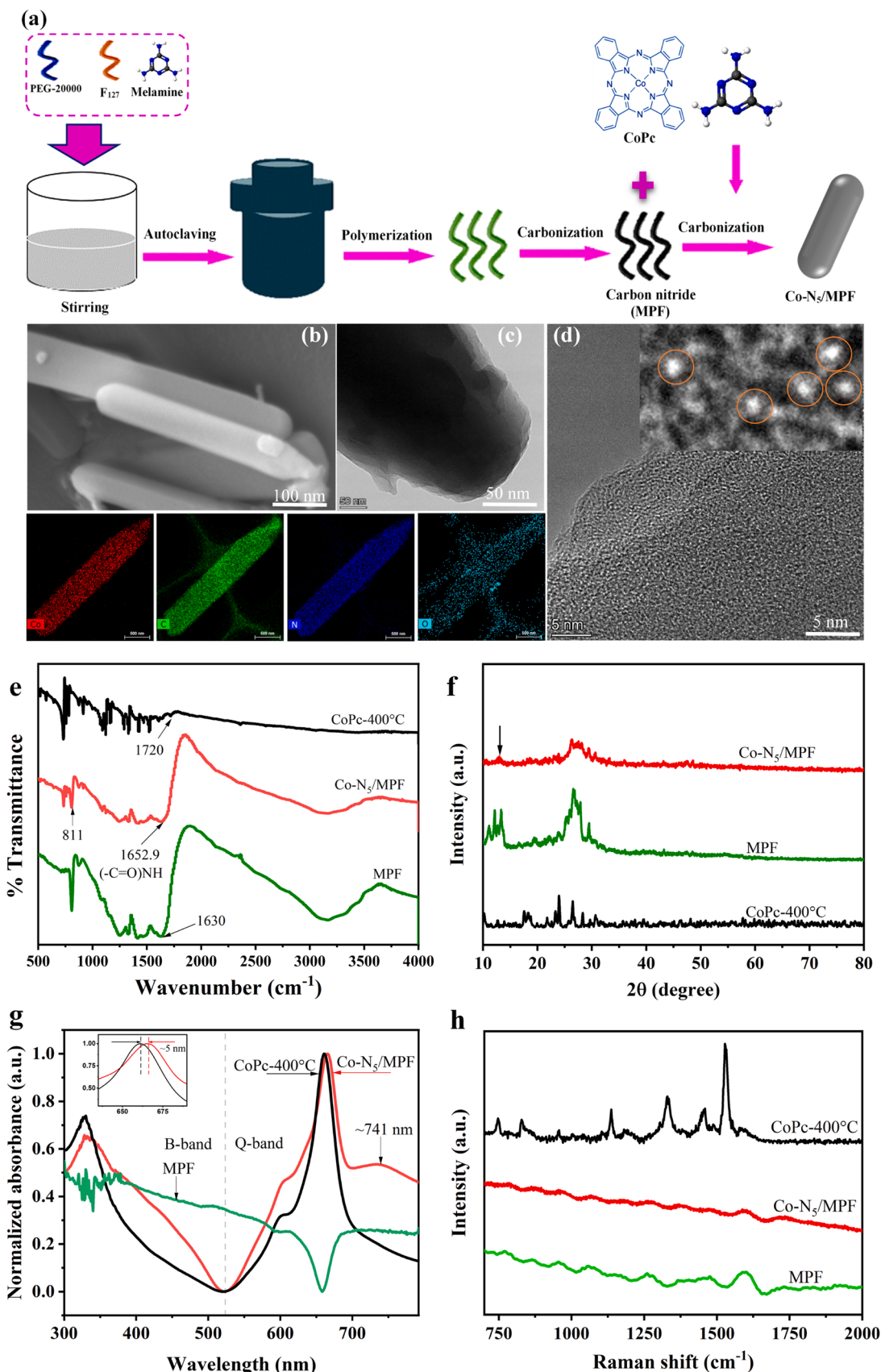


**Fig. 2.** Synthesis, morphology, and structural characterizations of MPF and Co-N<sub>5</sub>/MPF. (a) Schematic illustration of synthesis process of MPF and immobilization of CoPc in MPF. (b) SEM image of Co-N<sub>5</sub>/MPF and corresponding EDX mappings for C, N, O, and Co atoms. (c) TEM, and (d) HR-TEM image of Co-N<sub>5</sub>/MPF. (e) FTIR spectra, (f) XRD pattern, (g) UV-vis spectra, and (h) Raman spectra of MPF, CoPc-400 °C, and Co-N<sub>5</sub>/MPF.

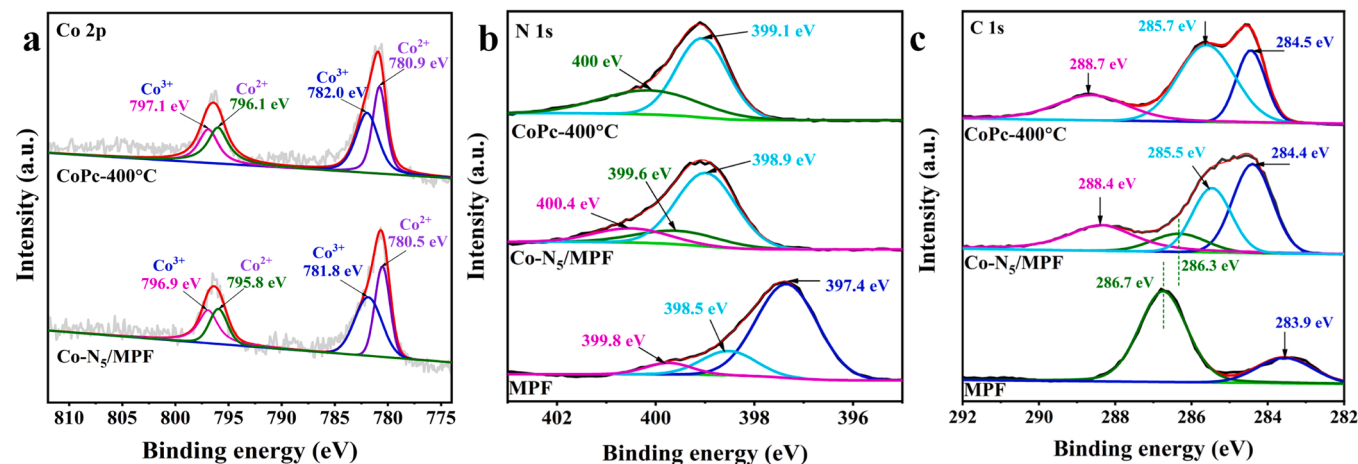


**Fig. 3.** High-resolution XPS spectrum comparison for (a) Co 2p in CoPc-400 °C and Co-N<sub>5</sub>/MPF, (b) N 1s and (c) C 1s in CoPc-400 °C, Co-N<sub>5</sub>/MPF and MPF.

ligand, leading to a decrease in electron density around Co atoms.

This observation corresponds to the UV-vis and FTIR results. Additionally, the high-resolution N 1s XPS spectra of the MPF sample were well deconvoluted into three peaks (Fig. 3b). The peak at 397.4 eV and 398.5 eV corresponded to sp<sup>2</sup>N<sub>1</sub> and sp<sup>2</sup>N<sub>2</sub>, respectively, and 399.8 eV was attributed to the -NH<sub>2</sub> or NH groups [56,61]. Moreover, the atomic N/C ratio (1.2), as determined by XPS analysis in MPF materials (Table S1), was in good agreement with the C<sub>3</sub>N<sub>4</sub> stoichiometry. Due to the different connection modes, the N 1s spectra of Co-N<sub>5</sub>/MPF varied considerably (Fig. 3b). The peak sp<sup>2</sup>N<sub>1</sub> disappeared owing to the formation of Co-Nx (399.6 eV) peak. A substantial intensity enhancement of the peak at 398.9 eV was ascribed to electron-withdrawing effect of cyanogen groups from MPF [57]. Besides, the C 1s spectrum of the MPF exhibited a sharp peak of C-NH<sub>2</sub> at 286.7 eV, which showed higher energy than the peak of C-C/C-H at 283.9 eV (Fig. 3c). It implies that the electronic density of the carbon was reduced by interaction with a more electronegative atom (nitrogen) so that the carbon was positively charged [58]. Compared with the CoPc-400 °C, the C 1s spectra of

Co-N<sub>5</sub>/MPF showed a slightly negative shift of binding energies of three peaks at 284.4, 285.5, and 288.4 eV, corresponding to C-C/C=C, C-O/C-N and C=O/C=N bond [62]. In addition, an accompanying weak peak at 286.3 eV was ascribed to C-NH<sub>2</sub> [63–65]. These results further suggest that the environmental coordination of CoPc has probably changed due to an electronic interaction between CoPc and MPF [23].

X-ray absorption spectroscopy (XAS) was conducted to elucidate local coordination environment and electronic structure of the Co species in Co-N<sub>5</sub>/MPF. For comparison, Co<sub>3</sub>O<sub>4</sub>, Co foil, and CoPc-400 °C were measured as reference samples. Compared with Co<sub>3</sub>O<sub>4</sub> and Co foil, pre-edge features of CoPc-400 °C and Co-N<sub>5</sub>/MPF were observed in the Co K-edge X-ray absorption near edge structure (XANES) spectra due to a 1s to 3d transition of square-planar coordination with D<sub>4h</sub> local symmetry (Fig. 4a) [66,67].

These pre-edge features (inset 2 magnified image Fig. 4a) are attributed to dipole forbidden (quadrupole) transitions and may also signify the hybridization of ligand states with the 3d empty states of

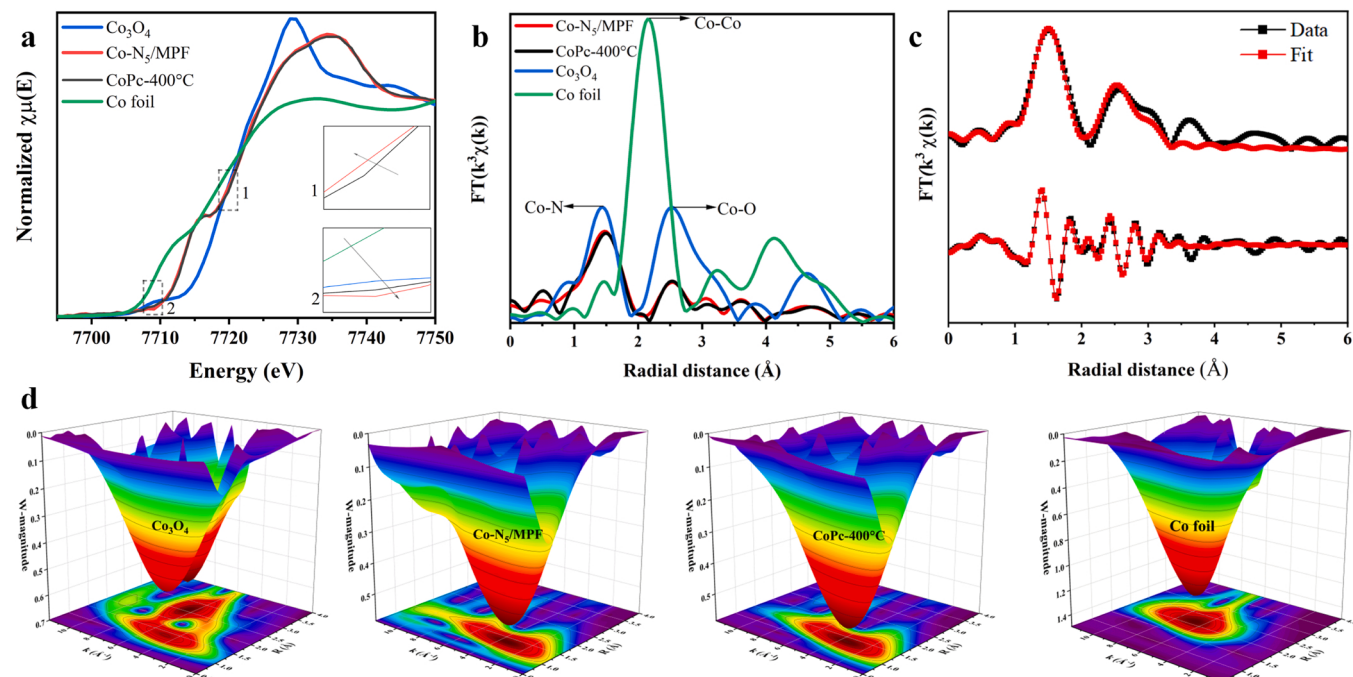


**Fig. 4.** (a) XANES (inset is the magnified image) and (b) FT-EXAFS in R space of Co<sub>3</sub>O<sub>4</sub>, Co foil, CoPc-400 °C, and Co-N<sub>5</sub>/MPF. (c) EXAFS fitting curves of the Co-N<sub>5</sub>/MPF. (d) WT- EXAFS of Co-N<sub>5</sub>/MPF along with reference samples at Co K-edge.

metal atom [75,76]. The Co in Co-N<sub>5</sub>/MPF exhibited a stronger pre-edge feature than that in CoPc-400 °C, suggesting strong hybridization of 3d and 2p states of the Co atom and N atom from MPF, respectively. It is expected that 3d and 2p orbital hybridization would tune electronic structure in the d-states of the Co atom [77,78]. What is more, it would facilitate trapping electrons from the Co atom giving rise to a deficit of electrons. As a result, its d-band center moved away from the Fermi level. These observations agree well with our DFT calculations (Fig. 1 and S1). The near edge feature in the Co K-edge XANES absorption threshold of Co-N<sub>5</sub>/MPF showed a negative shift relative to CoPc-400 °C (insert 1 magnified image Fig. 4a), suggesting a lower oxidation state, in good agreement with XPS results. The lower oxidation state of Co species in Co-N<sub>5</sub>/MPF also indicates strong electron delocalization owing to the presence of fifth N coordination. The Co K-edge of Fourier-transformed extended X-ray absorption fine structure (FT-EXAFS) revealed the prominent peaks at 1.47 and 1.50 Å in R space for Co-N<sub>5</sub>/MPF and CoPc-400 °C, respectively, corresponding to the Co-N bonding in the first shell (Fig. 4b). However, the bonding distance of Co-N in Co-N<sub>5</sub>/MPF showed a slight shift to a higher value than that of the Co-N<sub>4</sub> sample CoPc-400 °C (Table S3a~b), suggesting that Co atoms coordinated with additional N atoms. Additionally, the predominant peak at around 2.2 Å, attributed to the Co-Co bonding, was not detected for Co-N<sub>5</sub>/MPF (Fig. 4b). This inferred that the Co sites in Co-N<sub>5</sub>/MPF were in atomically dispersed form, which is in line with the above results of XRD and HRTEM (Fig. 2d and f). The FT-EXAFS results were corroborated by the wavelet transform WT-EXAFS at Co K-edge (Fig. 4d). Furthermore, the configuration of the Co atom in MPF was simulated via curve-fitting the FT-EXAFS spectra in the first shell using FEFFIT. The FT-EXAFS spectra of the Co-N<sub>5</sub>/MPF were well-fitted with five-coordinate Co, hence forming a Co-N<sub>5</sub> catalytic sites (Fig. 4c and S8 and Table S3a~b). These results provide solid evidence that Co sites in CoPc molecules effectively connected with MPF through axial N coordination, which could synergistically promote the charge transport of Co-N<sub>5</sub> catalytic site and MPF. That is, through a facile method and at mild temperature, molecules can

be homogeneously supported on the nitrogen-rich carbon nitride (polymer) materials as single atom Co catalysts with Co-N<sub>5</sub> catalytic site.

### 3.2. Electrochemical CO<sub>2</sub>RR of Co-N<sub>5</sub>/MPF catalyst

The CO<sub>2</sub>RR performance of Co-N<sub>5</sub>/MPF was evaluated in CO<sub>2</sub>-saturated 0.5 M KHCO<sub>3</sub> electrolyte in an H-type glass cell with three electrodes. As for control samples, CoPc-400 °C was used along with CoPc/MPF-500 °C and CoPc/MPF-600 °C, which were prepared from pyrolysis of CoPc/MPF. A high temperature above 400 °C was employed to clarify the active site of Co-N<sub>5</sub>/MPF in relation to structure performance. Fig. S3 shows structural changes determined by XRD for CoPc/MPF at each applied temperature. The linear sweep voltammetry (LSV) curves were used to study the activity of as-prepared catalysts, as illustrated in Fig. 5a. Co-N<sub>5</sub>/MPF exhibited a substantial current enhancement in CO<sub>2</sub>-saturated 0.5 M KHCO<sub>3</sub> electrolyte compared with that saturated by Ar gas (Fig. 5b), indicating a prominent catalytic effect of Co-N<sub>5</sub> catalytic site on the reduction of CO<sub>2</sub> in aqueous solution. Notably, Co-N<sub>5</sub>/MPF showed onset potential nearly around -0.3 V vs. RHE, corroborating that it had the highest electrocatalytic activity for CO<sub>2</sub>RR. Whereas, CoPc/MPF-500 °C and CoPc/MPF-600 °C showed onset potential at around -0.5 V vs. RHE and exhibited lower current density. As expected, CoPc in MPF at a high temperature above 400 °C underwent structural changes. Thus, all of the above data confirm that Co-N<sub>5</sub>/MPF has the best electrocatalytic activity and Co-N<sub>5</sub> is the real catalytic site for CO<sub>2</sub>RR. Concurrently, the stable and rapid increase in current density of Co-N<sub>5</sub>/MPF with the negative shift of potential compared with CoPc-400 °C, CoPc/MPF-500 °C and CoPc/MPF-600 °C indicated that MPF at 400 °C retained its stable 6π-electron system of the s-triazine rings for effectively stabilizing the CoPc molecules and thus improved its catalytic performance towards CO<sub>2</sub>RR. This study is consistent with those reported that CoPc is not stable due to its fast deactivation or structure changes at high reduction current density [9,42,68] (Fig. S9a).

To evaluate the product selectivity of as-synthesized catalysts, CO

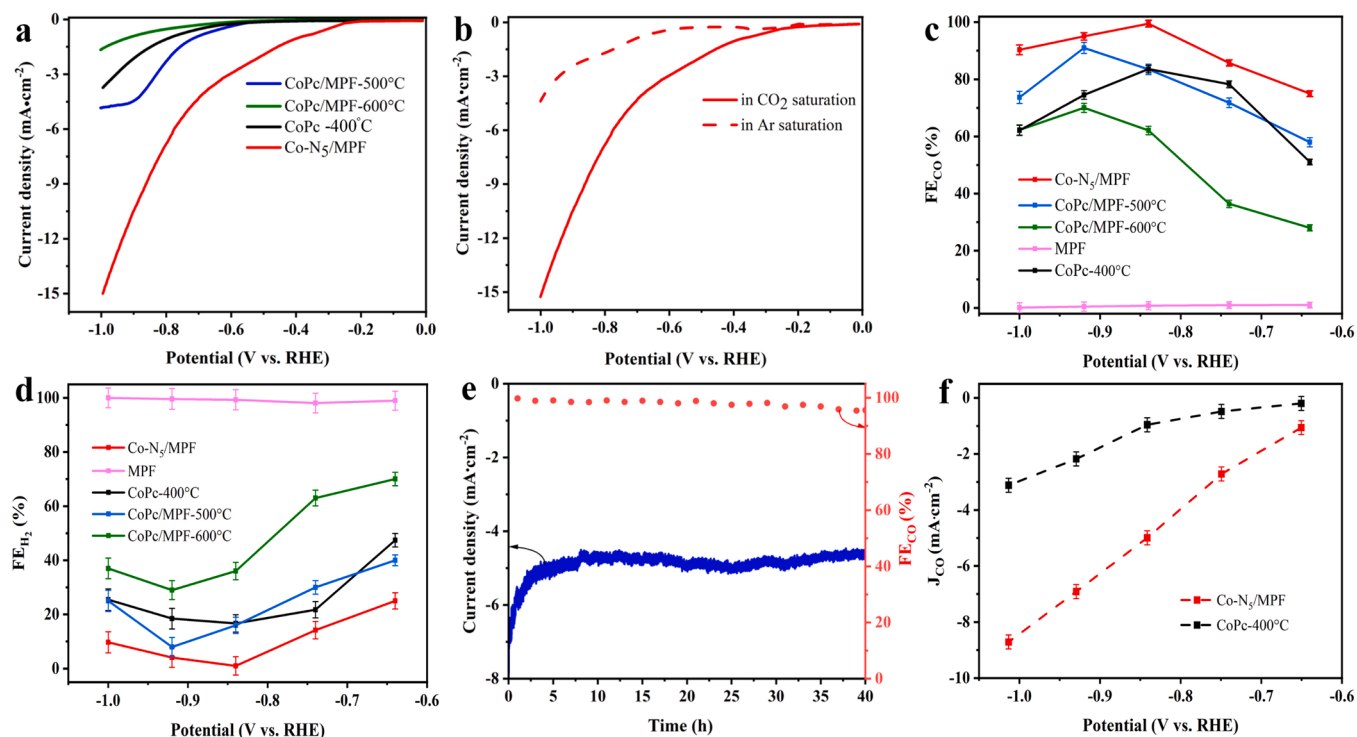


**Fig. 5.** CO<sub>2</sub>RR electrocatalytic performance. (a) LSV curves of Co-N<sub>5</sub>/MPF along with reference samples in CO<sub>2</sub> saturated 0.5 M KHCO<sub>3</sub> and (b) LSV curve comparison of Co-N<sub>5</sub>/MPF in CO<sub>2</sub> and Ar-saturated 0.5 M KHCO<sub>3</sub>. (c) FE of CO, and (d) FE of H<sub>2</sub>. (e) Long-term operation of Co-N<sub>5</sub>/MPF at -0.84 V vs. RHE. (f) CO partial current density of CoPc-400 °C, Co-N<sub>5</sub>/MPF at different applied potentials in 0.5 M KHCO<sub>3</sub>. Error bars correspond to the standard deviation of three measurements.

Faradaic efficiency ( $\text{FE}_{\text{CO}}$ ) was analysed by gas chromatography (GC) (see experimental section). The major gas products detected were CO and  $\text{H}_2$ , and no liquid products were detected. As shown in Fig. 5c, the  $\text{FE}_{\text{CO}}$  reached 99.5 % over Co-N<sub>5</sub>/MPF catalyst at  $-0.84 \text{ V}$  vs. RHE, which was significantly higher than that of CoPc-400 °C (83.6 %), CoPc/MPF-500 °C (83.5 %), and CoPc/MPF-600 °C (62.1 %) at the same potential. The hydrogen gas ( $\text{H}_2$ ) FE of Co-N<sub>5</sub>/MPF was much lower compared to those of its counterparts at all applied potentials (Fig. 5d). The successful inhibition of hydrogen evolution reaction was attributed to the good distribution of CoPc molecules in the MPF, as confirmed by HRTEM. All these contributed to the high selectivity of  $\text{CO}_2$  reduction over proton reduction of Co-N<sub>5</sub>/MPF catalyst [69]. Impressively, Co-N<sub>5</sub>/MPF catalyst could be recovered from the electrolysis mixture and reused at least three times without a dramatic decrease in catalytic performance (Table S4). Furthermore, the current density value, potential, and  $\text{FE}_{\text{CO}}$  remained nearly unchanged after electrolyzing 40 h at  $-0.84 \text{ V}$  vs. RHE (Fig. 5e, S9a, and b). A slight decrease in current density in the first hours during the stability test in Fig. 5e might be associated with a limiting current under a steady state whereby  $\text{H}_2$  permeated across the membrane was completely oxidized [79]. Additionally, after 40 h, its structure was almost unchanged (Fig. S9c). Also, there were no significant differences in the content of each element measured before and after the catalytic reaction (Table S5), signifying insignificant catalyst leaching into the electrolyte. This indicates a low chance of active site deactivation, leading to good stability of Co-N<sub>5</sub>/MPF catalyst. These results suggest that Co-N<sub>5</sub>/MPF had remarkable stability due to electron delocalization which prolonged carrier lifetime, increased electron density, and subsequently enabled rapid charge transfer [53,54]. The Co-N<sub>5</sub>/MPF showed 7-fold higher current densities ( $5.3 \text{ mA cm}^{-2}$ , normalized by the geometrical area) relative to that of CoPc-400 °C ( $0.9 \text{ mA cm}^{-2}$ ) at the potential of  $-0.84 \text{ V}$  vs. RHE (Fig. 5f). Such a current density and high  $\text{FE}_{\text{CO}}$  have seldom been reported under similar polymer supports (Table S6). On the other hand, the  $\text{FE}_{\text{CO}}$  increased to 90 % and 70 % at  $-0.92 \text{ V}$  vs. RHE for CoPc/MPF-500 °C and CoPc/MPF-600 °C, respectively. This phenomenon can be ascribed to different coordination environments of Co with nitrogen atoms, as reported that at 500 and 600 °C, the Co-N<sub>4</sub> and Co-N<sub>3</sub> catalysts were obtained, respectively [42]. Therefore, these results reveal that CoPc and MPF undergo structural changes at a high temperature above 400 °C (Fig. S3b), consistent with the previously reported studies [32,42]. Likewise, the  $\text{FE}_{\text{CO}}$  of Co-N<sub>5</sub>/MPF at an applied potential above  $-0.86 \text{ V}$  vs. RHE decreased, proposing structural change. The catalytic performance of standard CoPc and CoPc-400 °C is illustrated in Fig. S10. No noticeable difference was observed at optimal potential ( $-0.84 \text{ V}$  vs. RHE), suggesting little structural change in agreement with XRD and UV-vis results (Figs. S3d and S5).

Control experiments were conducted to explore the influence of MPF in catalytic reduction (Tables S7–S12). A bare MPF was prepared under the same conditions, and its catalytic performance was tested (Table S7). As shown in Fig. S10, its current density was small, and  $\text{FE}_{\text{CO}}$  was even much lower (< 2 %), inferring that MPF was not active for  $\text{CO}_2$  electroreduction. To demonstrate that the CO originates from  $\text{CO}_2$  reduction, a series of blank tests were conducted using 0.5 M KHCO<sub>3</sub> for the cases (1) bare carbon cloth and (2) Ar replacing  $\text{CO}_2$  in 0.5 M KHCO<sub>3</sub>. No carbon-containing compounds were detected in either of the cases, suggesting that  $\text{CO}_2$  reduction cannot proceed in the absence of Co-N<sub>5</sub>/MPF catalyst and  $\text{CO}_2$  is an essential ingredient for the production of CO gases. To verify the origin of CO, isotope-labelled carbon dioxide (<sup>13</sup>CO<sub>2</sub>) reduction was performed using 0.5 M KHCO<sub>3</sub> saturated with <sup>13</sup>CO<sub>2</sub> without catalyst (Fig. S11a) and with Co-N<sub>5</sub>/MPF catalyst (Fig. S11b). With Co-N<sub>5</sub>/MPF catalyst, a very strong signal of <sup>13</sup>CO at  $m/z = 29$  was detected, which confirmed the <sup>13</sup>CO generation is mostly originated from the <sup>13</sup>CO<sub>2</sub> reduction. Similarly, the role and influence of melamine on catalytic performance were investigated, as presented in Fig. S12a and b, which showed that the catalytic activity of Co-N<sub>5</sub>/MPF was slightly enhanced with the introduction of melamine. This might be

attributed to the excess availability of unsaturated nitrogen atoms as determined by XPS (22.6 at. %, Table S1), which possessed lone pairs of electrons beneficial for effectively resisting metal sintering due to a coordination reaction [70]. Moreover, the performance of bare melamine was tested as well (Table S9). Its current density was very small, and  $\text{FE}_{\text{CO}}$  was low (< 10 %), further confirming that Co-N<sub>5</sub> coordination was an active site and CO originated from CO<sub>2</sub>.

To figure out the origin of the excellent electrocatalytic activity of the hybrid catalyst, Nyquist plots were studied for Co-N<sub>5</sub>/MPF and CoPc-400 °C. As expected, Co-N<sub>5</sub>/MPF exhibited a lower impedance value than CoPc-400 °C (Fig. S10c). A relatively smaller charge transfer resistance boosts the formation of \*COOH intermediates, leading to improved CO<sub>2</sub>RR performance [80,81], in good agreement with our DFT calculations. A larger impedance value exhibited by CoPc-400 °C was attributed to high charge transfer resistance, possibly due to the reduced number of states around the Fermi level as demonstrated by PDOS (Fig. 1a). To elucidate the intrinsic activity of the Co-N<sub>5</sub>/MPF, turnover frequency (TOF) value for CO product at  $-0.84 \text{ V}$  vs. RHE was calculated to compare with those of standard CoPc and CoPc-400 °C catalyst. The Co-N<sub>5</sub>/MPF showed the highest TOF value (Fig. S11c,  $4.32 \text{ h}^{-1}$ ) among all the catalysts, whereas TOF values of standard CoPc ( $1.37 \text{ h}^{-1}$ ) and CoPc-400 °C ( $1.78 \text{ h}^{-1}$ ) are similar in value. Fig. S10d showed the Tafel plots of Co-N<sub>5</sub>/MPF with a slope of  $378 \text{ mV dec}^{-1}$  in the linear, lower current density regime ( $-0.6$  to  $-1.0 \text{ V}$ ). Tafel slope of Co-N<sub>5</sub>/MPF differed considerably from that of the CoPc-400 °C ( $282 \text{ mV dec}^{-1}$ ), suggesting CoPc in Co-N<sub>5</sub>/MPF might have a different structure. It influenced the mechanistic pathways for  $\text{CO}_2$  conversion by a different one from that pertains with the simple molecular analogous [17], and could also be associated with mass transport limitation [82].

### 3.3. Theoretical calculations

To further understand the intrinsic property and reactivity of Co-N<sub>5</sub>/MPF catalyst, the  $\text{CO}_2$  reduction reaction pathways were probed via computational hydrogen electrode (CHE) model (Fig. 6a). The energy barrier for Co-N<sub>5</sub>/MPF to convert  $\text{CO}_2$  to adsorbed \*COOH (0.28 eV) was exactly equal to the thermoneutral value, lower than that of CoPc (0.54 eV), and for \*CO species it was close to zero ( $-0.01 \text{ eV}$ ). Thus, it suggested that Co-N<sub>5</sub>/MPF catalyst surface facilitated the intermediate adsorption/desorption, which enhanced a faster CO<sub>2</sub>RR kinetics (Fig. 6b). The incredibly low barrier energy in the first step may be caused by electron delocalization of the Co-N<sub>5</sub> active site, which can modulate adsorption energy between key intermediate \*COOH and the active site of Co-N<sub>5</sub>/MPF catalyst. This makes the Co-N<sub>5</sub>/MPF show better CO<sub>2</sub>RR performance than that on CoPc. Moreover, the reaction pathway profiles for hydrogen evolution competitive reaction (HER) associated with these two models was conducted. As shown in Fig. 6c, Co-N<sub>5</sub>/MPF exhibited higher barrier energy of 1.25 eV for HER than that of CoPc (0.15 eV), suggesting significant inhibition of  $\text{H}_2$  generation from the reduction of protons in the aqueous electrolyte, in agreement with our experimental results.

To further insight into electron transfer, the planar-averaged charge density difference along  $z$  direction for CoPc and Co-N<sub>5</sub>/MPF along with electron localization function (ELF) was plotted in Fig. 6d and e. The positive and negative values represented electron accumulation and depletion, respectively. It can be seen that besides the two peaks exhibited by CoPc at around 5.4 and 4.5 Å in  $z$  direction corresponding to electron accumulation (Fig. 6d), the axial N was shown up to influence more significant electron accumulation peaks located at 5.1, 4.1, 2.5 and 1.5 Å in  $z$  direction for Co-N<sub>5</sub>/MPF (Fig. 6e). The strong interaction between Co atom and MPF for Co-N<sub>5</sub>/MPF through the axial N enabled charges transfer from Co site to MPF due to their differences in Fermi energy levels, which significantly enhanced the activity [71]. Thus, electron delocalization of Co-N<sub>5</sub> site of Co-N<sub>5</sub>/MPF played an important role in dictating the reaction performance [49,54]. Combined these data with the DOS analysis in Fig. 1b, the electrons were partially

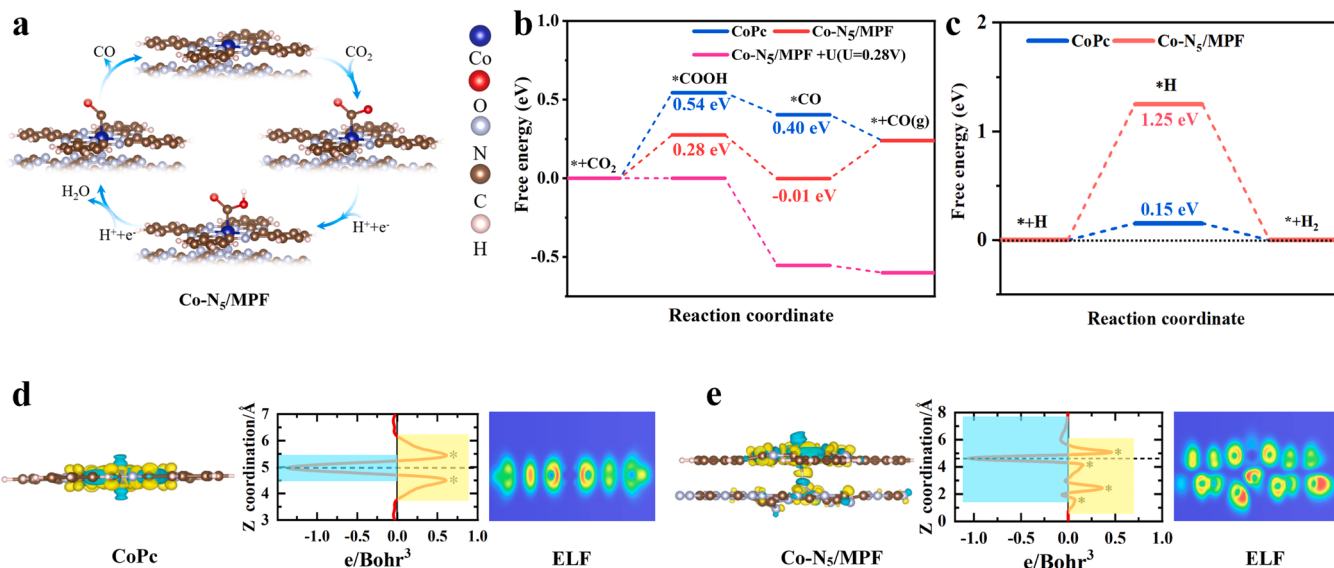


**Fig. 6.** (a) Optimized structures for the intermediates. (b) Free energy diagrams of CO<sub>2</sub>RR pathways for CoPc and Co-N<sub>5</sub>/MPF, (c) Calculated free energy of hydrogen adsorption on CoPc and Co-N<sub>5</sub>/MPF. (d, e) Planar-averaged charge density difference for Co-N<sub>5</sub>/MPF and CoPc. The yellow and cyan areas indicate electron accumulation and depletion, respectively.

withdrawn from Co-N<sub>4</sub> site to MPF through the axial N coordination, indicating electron delocalization of Co-N<sub>5</sub> site. These findings provide intrinsic elucidation that the downshift of the *d*-band center as the anti-bonding states of Co-N<sub>5</sub>/MPF are filled with more electrons due to electron delocalization, modulates the adsorption energy of \*COOH intermediates while facilitating the desorption energy of \*CO from the catalyst surface for CO<sub>2</sub>RR catalysis. Therefore, the remarkable electrocatalytic performance of Co-N<sub>5</sub>/MPF catalyst is well correlated to the electron delocalization.

#### 4. Conclusions

In summary, the effect of MPF as a *Supporting material* on the Co-N<sub>4</sub> local catalytic site under mild temperatures has been explored in detail. The robust interactions between CoPc and MPF through axial coordination lead to Co-N<sub>5</sub> catalytic site formation. The presence of MPF leads to electron delocalization on Co-N<sub>4</sub> site of CoPc, thus modulating its intrinsic electronic structure and, thereby *d*-band center, which enhances the conductivity and optimizes the interaction between the active sites and intermediates. Considerably, the Co-N<sub>5</sub>/MPF catalyst exhibits high activity and selectivity (FE<sub>CO</sub> > 99 %) for electrochemical CO<sub>2</sub> reduction and remarkable stability for 40 h. The catalytic selectivity is attributed to electron coupling between the *d*-states of Co and *p*-states of N ligands, which can enhance CO<sub>2</sub> activation, effectively decrease the energy barrier of intermediate \*COOH and boost desorption of CO as well. This work not only provides a strategy to design a low-cost and efficient electrocatalyst but also sheds light on expanding the applications of nitrogen-rich carbon nitride materials, which could pave a promising way for regulating M-N<sub>4</sub> catalytic active site owing to their unique thermal and chemically stable host-guest material at mild temperatures.

#### CRediT authorship contribution statement

**Jofrey Jackson Masana:** Investigation, Validation, Conceptualization, Methodology, Formal analysis, Data curation, Writing - Original Draft. **Jiayong Xiao:** Methodology, Software, Formal analysis, Data curation, Writing - Original Draft. **Hui Zhang:** Data curation. **Xiaoying Lu:** Writing - review & editing. **Ming Qiu:** Supervision, Project administration, Resources, Writing - review & editing. **Ying Yu:** Supervision, Project administration, Resources, Writing - review & editing.

#### Declaration of Competing Interest

The authors declare that they have no known competing financial interests or personal relationships that could have appeared to influence the work reported in this paper.

#### Data availability

Data will be made available on request.

#### Acknowledgments

This work was financially supported by the National Key Research and Development Program of China (2022YFB3803600), National Natural Science Foundation of China (Nos. U20A20246 and 51872108), the Fundamental Research Funds for the Central Universities (Innovation funded Projects) (No. 2022CXZZ104). We thank the XAFCA beamline of Singapore Synchrotron Light Source (SSL) for the support of XAS measurements.

#### Appendix A. Supporting information

Supplementary data associated with this article can be found in the online version at doi:10.1016/j.apcatb.2022.122199.

#### References

- [1] M. Wang, K. Torbensen, D. Salvatore, S. Ren, D. Joulié, F. Dumoulin, D. Mendoza, B. Lassalle-Kaiser, U. Isci, C.P. Berlinguet, M. Robert, CO<sub>2</sub> electrochemical catalytic reduction with a highly active cobalt phthalocyanine, *Nat. Commun.* 10 (2019) 3602, <https://doi.org/10.1038/s41467-019-11542-w>.
- [2] J. Chen, Z. Wang, H. Lee, J. Mao, C.A. Grimes, C. Liu, M. Zhang, Z. Lu, Y. Chen, S.-P. Feng, Efficient electroreduction of CO<sub>2</sub> to CO by Ag-decorated S-doped g-C<sub>3</sub>N<sub>4</sub>/CNT nanocomposites at industrial scale current density, *Mater. Today Phys.* 12 (2020), 100176, <https://doi.org/10.1016/j.mtphys.2019.100176>.
- [3] K. Huo, X. Liu, B. Wei, S. Zhang, H. Wang, Y. Sun, Research progress regarding transition metal-catalyzed carbonylations with CO<sub>2</sub>/H<sub>2</sub>, *Acta Phys. - Chim. Sin.* 37 (2021) 1–16, <https://doi.org/10.3866/PKU.WHXB202009098>.
- [4] H.M. Jhong, S. Ma, P.J.A. Kenis, Electrochemical conversion of CO<sub>2</sub> to useful chemicals: current status, remaining challenges, and future opportunities, *Curr. Opin. Chem. Eng.* 2 (2013) 191–199, <https://doi.org/10.1016/j.coche.2013.03.005>.
- [5] Z.W. Seh, J. Kibsgaard, C.F. Dickens, I. Chorkendorff, J.K. Nørskov, T.F. Jaramillo, Combining theory and experiment in electrocatalysis: Insights into materials design, *Science* 355 (2017) 146, <https://doi.org/10.1126/science.aad4998>.

- [6] J.J. Masana, B. Peng, Z. Shuai, M. Qiu, Y. Yu, Influence of halide ions on the electrochemical reduction of carbon dioxide over a copper surface, *J. Mater. Chem. A* 10 (2022) 1086–1104, <https://doi.org/10.1039/DITA09125E>.
- [7] J.P. Jones, G.K.S. Prakash, G.A. Olah, Electrochemical CO<sub>2</sub> reduction: recent advances and current trends, *Isr. J. Chem.* 54 (2014) 1451–1466, <https://doi.org/10.1002/ijch.201400081>.
- [8] Q. Zhou, W. Zhang, M. Qiu, Y. Yu, Role of oxygen in copper-based catalysts for carbon dioxide electrochemical reduction, *Mater. Today Phys.* 20 (2021), 100443, <https://doi.org/10.1016/j.mtphys.2021.100443>.
- [9] X. Zhang, Y. Wang, M. Gu, M. Wang, Z. Zhang, W. Pan, Z. Jiang, H. Zheng, M. Lucero, H. Wang, G.E. Sterbinsky, Q. Ma, Y.G. Wang, Z. Feng, J. Li, H. Dai, Y. Liang, Molecular engineering of dispersed nickel phthalocyanines on carbon nanotubes for selective CO<sub>2</sub> reduction, *Nat. Energy* 5 (2020) 684–692, <https://doi.org/10.1038/s41560-020-0667-9>.
- [10] C. Costentin, S. Drouet, M. Robert, J.M. Savéant, A local proton source enhances CO<sub>2</sub> electroreduction to CO by a molecular Fe catalyst, *Science* 338 (2012) 90–94, <https://doi.org/10.1126/science.1224581>.
- [11] N.M. Latiff, X. Fu, D.K. Mohamed, A. Veksha, M. Handayani, G. Lisa, Carbon based copper(II) phthalocyanine catalysts for electrochemical CO<sub>2</sub> reduction: Effect of carbon support on electrocatalytic activity, *Carbon* 168 (2020) 245–253, <https://doi.org/10.1016/j.carbon.2020.06.066>.
- [12] X. Zhang, Z. Wu, X. Zhang, L. Li, Y. Li, H. Xu, X. Li, X. Yu, Z. Zhang, Y. Liang, H. Wang, Highly selective and active CO<sub>2</sub> reduction electrocatalysts based on cobalt phthalocyanine/carbon nanotube hybrid structures, *Nat. Commun.* 8 (2017) 1–8, <https://doi.org/10.1038/ncomms14675>.
- [13] Z. Jiang, Y. Wang, X. Zhang, H. Zheng, X. Wang, Y. Liang, Revealing the hidden performance of metal phthalocyanines for CO<sub>2</sub> reduction electrocatalysis by hybridization with carbon nanotubes, *Nano Res.* 12 (2019) 2330–2334, <https://doi.org/10.1007/s12274-019-2455-z>.
- [14] K. Li, W. Wang, H. Zheng, X. Wang, Z. Xie, L. Ding, S. Yu, Y. Yao, F.-Y. Zhang, Visualizing highly selective electrochemical CO<sub>2</sub> reduction on a molecularly dispersed catalyst, *Mater. Today Phys.* 19 (2021), 100427, <https://doi.org/10.1016/j.mtphys.2021.100427>.
- [15] A. Mouchafi, T.K. Todorova, S. Dey, M. Fontecave, V. Mouge, A bioinspired molybdenum–copper molecular catalyst for CO<sub>2</sub> electroreduction, *Chem. Sci.* 11 (2020) 5503–5510, <https://doi.org/10.1039/DOSC01045F>.
- [16] A.M. Appel, J.E. Bercaw, A.B. Bocarsly, H. Dobbek, D.L. DuBois, M. Dupuis, J. G. Ferry, E. Fujita, R. Hille, P.J.A. Kenis, C.A. Kerfeld, R.H. Morris, C.H.F. Peden, A. R. Portis, S.W. Ragsdale, T.B. Rauchfuss, J.N.H. Reek, L.C. Seefeldt, R.K. Thauer, G. L. Waldrop, Frontiers, opportunities, and challenges in biochemical and chemical catalysis of CO<sub>2</sub> fixation, *Chem. Rev.* 113 (2013) 6621–6658, <https://doi.org/10.1021/cr300463y>.
- [17] S. Lin, C.S. Diercks, Y.B. Zhang, N. Kornienko, E.M. Nichols, Y. Zhao, A.R. Paris, D. Kim, P. Yang, O.M. Yaghi, C.J. Chang, Covalent organic frameworks comprising cobalt porphyrins for catalytic CO<sub>2</sub> reduction in water, *Science* 349 (2015) 1208–1213, <https://doi.org/10.1126/science.aac8343>.
- [18] W.W. Kramer, C.C.L. McCrory, Polymer coordination promotes selective CO<sub>2</sub> reduction by cobalt phthalocyanine, *Chem. Sci.* 7 (2016) 2506–2515, <https://doi.org/10.1039/C5SC04015A>.
- [19] N. Corbin, J. Zeng, K. Williams, K. Manthiram, Heterogeneous molecular catalysts for electrocatalytic CO<sub>2</sub> reduction, *Nano Res.* 12 (2019) 2093–2125, <https://doi.org/10.1007/s12274-019-2403-y>.
- [20] N. Han, Y. Wang, L. Ma, J. Wen, J. Li, H. Zheng, K. Nie, X. Wang, F. Zhao, Y. Li, J. Fan, J. Zhong, T. Wu, D.J. Miller, J. Lu, S.T. Lee, Y. Li, Supported cobalt polyphthalocyanine for high-performance electrocatalytic CO<sub>2</sub> reduction, *Chem* 3 (2017) 652–664, <https://doi.org/10.1016/j.chempr.2017.08.002>.
- [21] M. Zhu, J. Chen, L. Huang, R. Ye, J. Xu, Y.F. Han, Covalently grafting cobalt porphyrin onto carbon nanotubes for efficient CO<sub>2</sub> electroreduction, *Angew. Chem. Int. Ed.* 58 (2019) 6595–6599, <https://doi.org/10.1002/anie.201900499>.
- [22] M. Zhu, J. Chen, R. Guo, J. Xu, X. Fang, Y.F. Han, Cobalt phthalocyanine coordinated to pyridine-functionalized carbon nanotubes with enhanced CO<sub>2</sub> electroreduction, *Appl. Catal. B: Environ.* 251 (2019) 112–118, <https://doi.org/10.1016/j.apcatb.2019.03.047>.
- [23] C. He, Y. Zhang, Y. Zhang, L. Zhao, L.P. Yuan, J. Zhang, J. Ma, J.S. Hu, Molecular evidence for metallic cobalt boosting CO<sub>2</sub> electroreduction on pyridinic nitrogen, *Angew. Chem. Int. Ed.* 59 (2020) 4914–4919, <https://doi.org/10.1002/anie.201916520>.
- [24] S. Gong, W. Wang, X. Xiao, J. Liu, C. Wu, X. Lv, Elucidating influence of the existence formation of anchored cobalt phthalocyanine on electrocatalytic CO<sub>2</sub>-to-CO conversion, *Nano Energy* 84 (2021), 105904, <https://doi.org/10.1016/j.nano.2021.105904>.
- [25] C. Chen, X. Sun, D. Yang, L. Lu, H. Wu, L. Zheng, P. An, J. Zhang, B. Han, Enhanced CO<sub>2</sub> electroreduction: Via interaction of dangling S bonds and Co sites in cobalt phthalocyanine/ZnIn<sub>2</sub>S<sub>4</sub> hybrids, *Chem. Sci.* 10 (2019) 1659–1663, <https://doi.org/10.1039/C8SC03986K>.
- [26] R. Verma, R. Belgamwar, V. Polshettiwar, Plasmonic photocatalysis for CO<sub>2</sub> conversion to chemicals and fuels, *ACS Mater. Lett.* 3 (2021) 574–598, <https://doi.org/10.1021/acsmaterialslett.1c00081>.
- [27] Y.M. Zhang, L. Yan, M.X. Guan, D.Q. Chen, Z. Xu, H.Z. Guo, S.Q. Hu, S.J. Zhang, X. B. Liu, Z.X. Guo, S.F. Li, S. Meng, Indirect to direct charge transfer transition in plasmon-enabled CO<sub>2</sub> photoreduction, *Adv. Sci.* 9 (2021) 2102978, <https://doi.org/10.1002/advs.202102978>.
- [28] F.K. Kessler, Y. Zheng, D. Schwarz, C. Merschjann, W. Schnick, X. Wang, M. J. Bojdys, Functional carbon nitride materials—design strategies for electrochemical devices, *Nat. Rev. Mater.* 2 (2017) 17030, <https://doi.org/10.1038/natrevmats.2017.30>.
- [29] J.R. Holst, E.G. Gillan, From triazines to heptazines: deciphering the local structure of amorphous nitrogen-rich carbon nitride materials, *J. Am. Chem. Soc.* 130 (2008) 7373–7379, <https://doi.org/10.1021/ja709992s>.
- [30] X. Dai, Z. Li, Y. Ma, M. Liu, K. Du, H. Su, H. Zhuo, L. Yu, H. Sun, X. Zhang, Metallic cobalt encapsulated in bamboo-like and nitrogen-rich carbonitride nanotubes for hydrogen evolution reaction, *ACS Appl. Mater. Interfaces* 8 (2016) 6439–6448, <https://doi.org/10.1021/acsami.5b11717>.
- [31] X. Zou, X. Huang, A. Goswami, R. Silva, B.R. Sathe, E. Mikmekov, T. Asefa, Cobalt-embedded nitrogen-rich carbon nanotubes efficiently catalyze hydrogen evolution reaction at all pH values, *Angew. Chem. Int. Ed.* 53 (2014) 4372–4376, <https://doi.org/10.1002/anie.201311111>.
- [32] M. Kawaguchi, K. Nozaki, Synthesis, structure, and characteristics of the new host Material [(C<sub>3</sub>N<sub>3</sub>)<sub>2</sub>(NH)<sub>3</sub>]n, *Chem. Mater.* 7 (1995) 257–264, <https://doi.org/10.1021/cm00050a005>.
- [33] Y. Zhang, Q. Pan, G. Chai, M. Liang, G. Dong, Q. Zhang, J. Qiu, Synthesis and luminescence mechanism of multicolor-emitting g-C<sub>3</sub>N<sub>4</sub> nanopowders by low temperature thermal condensation of melamine, *Sci. Rep.* 3 (2013) 1–8, <https://doi.org/10.1038/srep01943>.
- [34] A. Thomas, A. Fischer, F. Goettmann, M. Antonietti, J.O. Muller, R. Schlogl, J. M. Carlsson, Graphitic carbon nitride materials: variation of structure and morphology and their use as metal-free catalysts, *J. Mater. Chem.* 18 (2008) 4893–4908, <https://doi.org/10.1039/B800274F>.
- [35] G. Lalande, R. Cote, G. Tamizhmani, D. Guay, J.P. Dodelet, L. Dignard-Bailey, L. T. Weng, P. Bertran, Physical, chemical and electrochemical characterization of heat-treated tetracarboxylic cobalt phthalocyanine adsorbed on carbon black as electrocatalyst for oxygen reduction in polymer electrolyte fuel cells, *Electrochim. Acta* 40 (1995) 2635–2646, [https://doi.org/10.1016/0013-4686\(95\)00104-M](https://doi.org/10.1016/0013-4686(95)00104-M).
- [36] B.N. Achar, K.S. Lokesh, G.M. Fohlen, T.M.M. Kumar, Characterization of cobalt phthalocyanine sheet polymer by gas chromatography mass spectrometry on its pyrolysis products, *React. Funct. Polym.* 63 (2005) 63–69, <https://doi.org/10.1016/j.reactfunctpolym.2005.02.007>.
- [37] L. Dignard-Bailey, M.L. Trudeau, A. Joly, R. Schulz, G. Lalande, D. Guay, J. P. Dodelet, Graphitization and particle size analysis of pyrolyzed cobalt phthalocyanine / carbon catalysts for oxygen reduction in fuel cells, *J. Mater. Res.* 9 (1994) 3203–3209, <https://doi.org/10.1557/JMR.1994.3203>.
- [38] P. Zhou, L. Jiang, F. Wang, K. Deng, K. Lv, Z. Zhang, High performance of a cobalt–nitrogen complex for the reduction and reductive coupling of nitro compounds to amines and their derivatives, *Sci. Adv.* 3 (2017) 1–11, <https://doi.org/10.1126/sciadv.1601919>.
- [39] M. Scardamaglia, C. Struzzi, S. Lizzit, M. Dalmiglio, P. Lacovic, A. Baraldi, C. Mariani, M.G. Betti, Energetics and hierarchical interactions of metal-phthalocyanines adsorbed on graphene/Ir(111), *Langmuir* 29 (2013) 10440–10447, <https://doi.org/10.1021/la401850v>.
- [40] A. Sabik, F. Golek, G. Antczak, Thermal desorption and stability of cobalt phthalocyanine on Ag(100), *Appl. Surf. Sci.* 435 (2018) 894–902, <https://doi.org/10.1016/j.apsusc.2017.11.149>.
- [41] J. Liu, S. Zhang Qiao, H. Liu, J. Chen, A. Orpe, D. Zhao, G.Q. Lu, Extension of the stöber method to the preparation of monodisperse resorcinol-formaldehyde resin polymer and carbon spheres, *Angew. Chem. Int. Ed.* 50 (2011) 5947–5951, <https://doi.org/10.1002/anie.201102011>.
- [42] Y. Pan, R. Lin, Y. Chen, S. Liu, W. Zhu, X. Cao, W. Chen, K. Wu, W.C. Cheong, Y. Wang, L. Zheng, J. Luo, Y. Lin, Y. Liu, C. Liu, J. Li, Q. Lu, X. Chen, D. Wang, Q. Peng, C. Chen, Y. Li, Design of single-atom Co-N<sub>5</sub> catalytic site: a robust electrocatalyst for CO<sub>2</sub> reduction with nearly 100% CO selectivity and remarkable stability, *J. Am. Chem. Soc.* 140 (2018) 4218–4221, <https://doi.org/10.1021/jacs.8b00814>.
- [43] K. Ham, D. Shin, J. Lee, The role of lone-pair electrons in Pt–N interactions for the oxygen reduction reaction in polymer exchange membrane fuel cells, *ChemSusChem* 13 (2020) 1751–1758, <https://doi.org/10.1002/cssc.201903403>.
- [44] B. Ravel, M. Newville, Athena, artemis, hephaestus: Data analysis for X-ray absorption spectroscopy using IFEFFIT, *J. Synchrotron Radiat.* 12 (2005) 537–541, <https://doi.org/10.1107/S0909049505012719>.
- [45] G. Kresse, J. Hafner, Ab initio molecular-dynamics simulation of the liquid-metalamorphous-semiconductor transition in germanium, *Phys. Rev. B* 49 (1994) 14251–14269, <https://doi.org/10.1103/PhysRevB.49.14251>.
- [46] P.E. Blöchl, Projector augmented-wave method, *Phys. Rev. B* 50 (1994) 17953–17979, <https://doi.org/10.1103/PhysRevB.50.17953>.
- [47] J.P. Perdew, K. Burke, M. Ernzerhof, Generalized gradient approximation made simple, *Phys. Rev. Lett.* 77 (1996) 3865–3868, <https://doi.org/10.1103/PhysRevLett.77.3865>.
- [48] Z. Zhu, Z. Li, J. Wang, R. Li, H. Chen, Y. Li, J.S. Chen, R. Wu, Z. Wei, Improving NiNx and pyridinic N active sites with space-confined pyrolysis for effective CO<sub>2</sub> electroreduction, *eScience* 22 (2022) 202205002, <https://doi.org/10.1016/j.esci.2022.05.002>.
- [49] K. Ding, J. Hu, W. Jin, L. Zhao, Y. Liu, Z. Wu, B. Weng, H. Hou, X. Ji, Dianion induced electron delocalization of trifunctional electrocatalysts for rechargeable Zn-air batteries and self-powered water splitting, *Adv. Funct. Mater.* (2022) 2201944, <https://doi.org/10.1002/adfm.202201944>.
- [50] H. Xin, A. Holewinski, N. Schweitzer, E. Nikolla, S. Linic, Electronic structure engineering in heterogeneous catalysis: Identifying novel alloy catalysts based on rapid screening for materials with desired electronic properties, *Top. Catal.* 55 (2012) 376–390, <https://doi.org/10.1007/s11244-012-9794-2>.
- [51] Z. Chen, Y. Song, J. Cai, X. Zheng, D. Han, Y. Wu, Y. Zang, S. Niu, Y. Liu, J. Zhu, X. Liu, G. Wang, Tailoring the d-band centers enables Co<sub>4</sub>N nanosheets to be highly active for hydrogen evolution catalysis, *Angew. Chem. Int. Ed.* 57 (2018) 5076–5080, <https://doi.org/10.1002/anie.201801834>.

- [52] S. Bhattacharjee, U.V. Waghmare, S.C. Lee, An improved d-band model of the catalytic activity of magnetic transition metal surfaces, *Sci. Rep.* 6 (2016) 1–10, <https://doi.org/10.1038/srep35916>.
- [53] H. Li, Y. Han, H. Zhao, W. Qi, D. Zhang, Y. Yu, W. Cai, S. Li, J. Lai, B. Huang, L. Wang, Fast site-to-site electron transfer of high-entropy alloy nanocatalyst driving redox electrocatalysis, *Nat. Commun.* 11 (2020) 1–9, <https://doi.org/10.1038/s41467-020-19277-9>.
- [54] M.L. Aubrey, B.M. Wiers, S.C. Andrews, T. Sakurai, S.E. Reyes-Lillo, S.M. Hamed, C. Yu, L.E. Darago, J.A. Mason, J. Baeg, F. Grandjean, G.J. Long, S. Seki, J. B. Neaton, P. Yang, J.R. Long, Electron delocalization and charge mobility as a function of reduction in metal-organic framework, *Nat. Mater.* 17 (2018) 625–632, <https://doi.org/10.1038/s41563-018-0098-1>.
- [55] S. Matsumoto, K.K. Chattopadhyay, M. Mieno, T. Ando, An attempt to prepare carbon nitride by thermal plasma chemical vapor deposition from graphite and nitrogen, *J. Mater. Res.* 13 (1998) 180–186, <https://doi.org/10.1557/JMR.1998.0024>.
- [56] Q. Guo, Y. Xie, X. Wang, S. Lv, T. Hou, X. Liu, Characterization of well-crystallized graphitic carbon nitride nanocrystallites via a benzene-thermal route at low temperatures, *Chem. Phys. Lett.* 380 (2003) 84–87, <https://doi.org/10.1016/j.cplett.2003.09.009>.
- [57] P. Kumar, A. Kumar, B. Sreedhar, B. Sain, S.S. Ray, S.L. Jain, Cobalt phthalocyanine immobilized on graphene oxide: an efficient visible-active catalyst for the photoreduction of carbon dioxide, *Chem. Eur. J.* 20 (2014) 6154–6161, <https://doi.org/10.1002/chem.201304189>.
- [58] M. Kawaguchi, S. Yagi, H. Enomoto, Chemical preparation and characterization of nitrogen-rich carbon nitride powders, *Carbon* 42 (2004) 345–350, <https://doi.org/10.1016/j.carbon.2003.11.004>.
- [59] J. Xu, H. Wang, C. Zhang, X. Yang, S. Cao, J. Yu, M. Shalom, From millimeter to subnanometer: Vapor-solid deposition of carbon nitride hierarchical nanostructures directed by supramolecular assembly, *Angew. Chem. Int. Ed.* 56 (2017) 8426–8430, <https://doi.org/10.1002/anie.201611946>.
- [60] Z. Han, X. Han, X. Zhao, J. Yu, H. Xu, Iron phthalocyanine supported on amidoximated PAN fiber as effective catalyst for controllable hydrogen peroxide activation in oxidizing organic dyes, *J. Hazard. Mater.* 320 (2016) 27–35, <https://doi.org/10.1016/j.jhazmat.2016.08.004>.
- [61] J. Yang, X. Wu, X. Li, Y. Liu, M. Gao, X. Liu, L. Kong, S. Yang, Synthesis and characterization of nitrogen-rich carbon nitride nanobelts by pyrolysis of melamine, *Appl. Phys. A* 105 (2011) 161–166, <https://doi.org/10.1007/s00339-011-6471-4>.
- [62] D. Guo, J. Zhang, G. Liu, X. Luo, F. Wu, Cobalt phthalocyanine-based nanodots as efficient catalysts for chemical conversion of CO<sub>2</sub> under ambient conditions, *J. Mater. Sci.* 56 (2021) 10990–10999, <https://doi.org/10.1007/s10853-021-05964-5>.
- [63] X. Guo, L. Rao, P. Wang, L. Zhang, Y. Wang, Synthesis of porous boron-doped carbon nitride: Adsorption capacity and photo-regeneration properties, *Int. J. Environ. Res. Public Heal* 16 (2019) 581, <https://doi.org/10.3390/ijerph16040581>.
- [64] C. Xu, K. Li, W. Zhang, Enhancing visible light photocatalytic activity of nitrogen-deficient g-C<sub>3</sub>N<sub>4</sub> via thermal polymerization of acetic acid-treated melamine, *J. Colloid Interface Sci.* 495 (2017) 27–36, <https://doi.org/10.1016/j.jcis.2017.01.111>.
- [65] S.C. Yan, Z.S. Li, Z.G. Zou, Photodegradation of rhodamine B and methyl orange over boron-doped g-C<sub>3</sub>N<sub>4</sub> under visible light irradiation, *Langmuir* 26 (2010) 3894–3901, <https://doi.org/10.1021/la904023j>.
- [66] G. Rossi, F. D'Acapito, L. Amidani, F. Boscherini, M. Pedio, Local environment of metal ions in phthalocyanines: K-edge X-ray absorption spectra, *Phys. Chem. Chem. Phys.* 18 (2016) 23686–23694, <https://doi.org/10.1039/C6CP04022E>.
- [67] A. Kumar, V.Q. Bui, J. Lee, L. Wang, A.R. Jadhav, X. Liu, X. Shao, Y. Liu, J. Yu, Y. Hwang, H.T.D. Bui, S. Ajmal, M.G. Kim, S.G. Kim, G.S. Park, Y. Kawazoe, H. Lee, Moving beyond bimetallic-alloy to single-atom dimer atomic-interface for all-pH hydrogen evolution, *Nat. Commun.* 12 (2021) 1–10, <https://doi.org/10.1038/s41467-021-27145-3>.
- [68] Y. Wu, Z. Jiang, X. Lu, Y. Liang, H. Wang, Domino electroreduction of CO<sub>2</sub> to methanol on a molecular catalyst, *Nature* 575 (2019) 639–642, <https://doi.org/10.1038/s41586-019-1760-8>.
- [69] I. Hod, O.K. Farha, J.T. Hupp, Powered by porphyrin packing, *Nat. Mater.* 14 (2015) 1192–1193, <https://doi.org/10.1038/nmat4494>.
- [70] J. Sun, Q. Xu, J. Qi, D. Zhou, H. Zhu, J.Z. Yin, Isolated single atoms anchored on N-doped carbon materials as a highly efficient catalyst for electrochemical and organic reactions, *ACS Sustain. Chem. Eng.* 8 (2020) 14630–14656, <https://doi.org/10.1021/acssuschemeng.0c04324>.
- [71] M.J. Zachman, V. Fung, F. Polo-Garzon, S. Cao, J. Moon, Z. Huang, D. Jiang, Z. Wu, M. Chi, Measuring and directing charge transfer in heterogenous catalysts, *Nat. Commun.* 13 (2022) 3253, <https://doi.org/10.1038/s41467-022-30923-2>.
- [72] J. Chen, J.C.S. Wu, P.C. Wu, D.P. Tsai, Plasmonic photocatalyst for H<sub>2</sub> evolution in photocatalytic water splitting, *J. Phys. Chem. C* 115 (2011) 210–216, <https://doi.org/10.1021/jp1074048>.
- [73] J. Fang, S. Cao, Z. Wang, M.M. Shahjamali, S.C.J. Loo, J. Barber, C. Xue, Mesoporous plasmonic Au-TiO<sub>2</sub> nanocomposites for efficient visible-light-driven photocatalytic water reduction, *Int. J. Hydrol. Energy* 37 (2012) 17853–17861, <https://doi.org/10.1016/j.ijhydene.2012.09.023>.
- [74] Y. Lum, J.W. Ager, Stability of residual oxides in oxide-derived copper catalysts for electrochemical CO<sub>2</sub> reduction investigated with <sup>18</sup>O labeling, *Angew. Chem. Int. Ed.* 57 (2018) 551–554, <https://doi.org/10.1002/anie.201710590>.
- [75] K. Frank, E. Koch, H. Biester, Observation of in situ formation of phthalocyanine-bis (pyridine) iron(ii) by x-ray absorption spectroscopy, *J. Phys.* 47 (1986) 653–657, <https://doi.org/10.1051/jphyscol:19868124>.
- [76] C.N. Kodituwakk, C.A. Burns, A.H. Said, H. Sinn, X. Wang, T. Gog, D.M. Casa, M. Tuel, Resonant inelastic x-ray scattering studies of the organic semiconductor copper phthalocyanine, *Phys. Rev. B* 77 (2008), 125205, <https://doi.org/10.1103/PhysRevB.77.125205>.
- [77] M.G. Betti, P. Gargiani, C. Mariani, S. Turchini, N. Zema, S. Fortuna, A. Calzolari, S. Fabris, Formation of hybrid electronic states in FePc chains mediated by the Au(110) surface, *J. Phys. Chem. C* 116 (2012) 8657–8663, <https://doi.org/10.1021/jp300663t>.
- [78] I.E. Brumboiu, S. Haldar, J. Lüder, O. Eriksson, H.C. Herper, B. Brenna, B. Sanyal, *J. Chem. Theory Comput.* 12 (2016) 1772–1785, <https://doi.org/10.1021/acs.jctc.6b00091>.
- [79] J. Zhang, H. Zhang, J. Wu, J. Zhang, PEM Fuel Cell Testing and Diagnosis, Elsevier B.V., 2013, pp. 1–375, <https://doi.org/10.1016/C2009-0-63216-5>.
- [80] Z. Yang, H. Wang, X. Fei, W. Wang, Y. Zhao, X. Wang, X. Tan, Q. Zhao, H. Wang, J. Zhu, L. Zhou, H. Ning, M. Wu, MOF derived bimetallic CuBi catalysts with ultra-wide potential window for high-efficient electrochemical reduction of CO<sub>2</sub> to formate, *Appl. Catal. B: Environ.* 298 (2021), 120571, <https://doi.org/10.1016/j.apcatb.2021.120571>.
- [81] Y. Xiong, B. Wei, M. Wu, B. Hu, F. Zhu, J. Hao, W. Shi, Rapid synthesis of amorphous bimetallic copper-bismuth electrocatalysts for efficient electrochemical CO<sub>2</sub> reduction to formate in a wide potential window, *J. CO<sub>2</sub> Util.* 51 (2021), 101621, <https://doi.org/10.1016/j.jcou.2021.101621>.
- [82] A.N. Marianov, Y.J. Jiang, Covalent ligation of Co molecular catalyst to carbon cloth for efficient electroreduction of CO<sub>2</sub> in water, *Appl. Catal. B: Environ.* 244 (2019) 881–888, <https://doi.org/10.1016/j.apcatb.2018.11.084>.